High-Resolution Images of Retinal Structure in Patients with Choroideremia

Reema Syed,[1] Sanna M. Sundquist,[1] Kavitha Ratnam,[1] Shiri Zayit-Soudry,[1] Yuhua Zhang,[2] J. Brooks Crawford,[1] Ian M. MacDonald,[3] Pooja Godara,[4] Jungtae Rha,[4] Joseph Carroll,[4–6] Austin Roorda,[7] Kimberly E. Stepien,[4] and Jacque L. Duncan[1]

PURPOSE. To study retinal structure in choroideremia patients and carriers using high-resolution imaging techniques.

METHODS. Subjects from four families (six female carriers and five affected males) with choroideremia (CHM) were characterized with best-corrected visual acuity (BCVA), kinetic and static perimetry, full-field electroretinography, and fundus autofluorescence (FAF). High-resolution macular images were obtained with adaptive optics scanning laser ophthalmoscopy (AOSLO) and spectral domain optical coherence tomography (SD-OCT). Coding regions of the *CHM* gene were sequenced.

RESULTS. Molecular analysis of the *CHM* gene identified a deletion of exons 9 to 15 in family A, a splice site mutation at position 79+1 of exon 1 in family B, deletion of exons 6 to 8 in family C, and a substitution at position 106 causing a premature stop in family D. BCVA ranged from 20/16 to 20/63 in carriers and from 20/25 to 5/63 in affected males. FAF showed abnormalities in all subjects. SD-OCT showed outer retinal layer loss, outer retinal tubulations at the margin of outer retinal loss, and inner retinal microcysts. Patchy cone loss was present in two symptomatic carriers. In two affected males, cone mosaics were disrupted with increased cone spacing near the fovea but more normal cone spacing near the edge of atrophy.

CONCLUSIONS. High-resolution retinal images in CHM carriers and affected males demonstrated RPE and photoreceptor cell degeneration. As both RPE and photoreceptor cells were affected, these cell types may degenerate simultaneously in CHM. These findings provide insight into the effect of *CHM* mutations on macular retinal structure, with implications for the development of treatments for CHM. (ClinicalTrials.gov number, NCT00254605.) (*Invest Ophthalmol Vis Sci.* 2013; 54:950–961) DOI:10.1167/iovs.12-10707

Choroideremia (CHM) is an X-linked disorder causing progressive degeneration of the retina, RPE, and choroid. Affected males develop night blindness in childhood with progressive peripheral vision loss and central vision loss in advanced disease. Female carriers may be asymptomatic but typically show patchy pigmentary abnormalities in the peripheral fundus.[1] Disease severity in female carriers is variable due to lyonization, where one X chromosome is randomly inactivated in each cell early in fetal development.[2] Cells expressing the mutant X-chromosome are interspersed with cells expressing the normal X-chromosome, creating a mosaic pattern with the proportion of cells expressing the mutant X-chromosome determining the extent and severity of disease.[3]

Identification of the gene responsible for CHM[4–6] (*CHM,* also known as *REP-1,* MIM 300390) has facilitated understanding of CHM disease pathogenesis through animal models,[5,6] and has accelerated the development of human clinical trials for CHM, including lutein supplementation,[7] neurotrophic factor therapy,[8] and the initiation of a gene replacement therapy clinical trial (www.clinicaltrials.gov, NCT01461213; MacLaren RE, et al. *IOVS* 2012;53:ARVO E-Abstract 5577). Despite this progress, the mechanism of retinal degeneration in CHM remains incompletely understood. *CHM* encodes Rab Escort Protein-1 (REP-1),[4] a protein that facilitates posttranslational modification of Rab proteins, which regulate intracellular trafficking.[9,10] Mutations in the *CHM* gene create stop codons that result in the truncation or absence of REP-1 protein.[11,12] Although the *CHM* gene is expressed in all cells, typically pathology is limited to ocular tissues in CHM patients. An autosomal gene with significant homology to *CHM* encodes Rab escort protein-2 (REP-2), and the tissue-specific expression of these two genes may be necessary for normal Rab protein prenylation.[13,14] The primary site of degeneration in CHM remains unclear. Histological studies of a male patient[14]

showed photoreceptor and RPE cell loss, but did not include data demonstrating normal photoreceptors and abnormal RPE; while in female carriers[15,16] and a mouse model of CHM,[17] the RPE and photoreceptors show independent cell loss; when the gene responsible for CHM is knocked out in both photoreceptors and RPE cells independently in mice, the dynamics of the degenerative process are accelerated, suggesting that RPE disease accelerates photoreceptor degeneration.[17]

Histologic reports of CHM patients can provide vital information on the pathogenesis of the disease, but most eyes studied have had advanced disease,[18-20] whereas animal models of CHM may not mimic the human disease precisely. We sought to characterize macular retinal structure with high resolution in living CHM patients and carriers with a range of disease severity. Given recent reports of retinal remodeling in CHM patients,[21] analysis of the cone photoreceptor mosaic at different stages of disease could provide additional insight into the effect *CHM* mutations have on photoreceptor degeneration, and may provide a sensitive outcome measure of disease progression and therapeutic effect as clinical trials for CHM are initiated.

Adaptive optics scanning laser ophthalmoscopy (AOSLO) allows for direct visualization of the cone mosaic in living eyes by compensating for ocular optical aberrations.[22] Used in conjunction with other imaging and diagnostic techniques, AOSLO allows comparison of cone spacing with normal subjects and can provide insight into the effects of different retinal degenerations on macular cones.[23-28] The present study acquired high-resolution retinal images with AOSLO and spectral domain optical coherence tomography (SD-OCT) to evaluate retinal structure in living eyes with CHM to assess whether photoreceptors or RPE cells degenerate primarily, independently, or simultaneously.

METHODS

Research procedures followed the tenets of the Declaration of Helsinki and informed consent was obtained from all subjects. The study protocol was approved by the institutional review boards of the University of California, San Francisco, the University of California, Berkeley, and the Medical College of Wisconsin.

Subjects

Eleven subjects from four unrelated families, including five affected males and six female carriers, were characterized clinically (Fig. 1). Three subjects (one affected male, A-IV-3, and two female carriers, A-III-1 and A-V-2) were from family A; four subjects (two males, B-IV-2 and B-IV-3, and two female carriers, B-V-3 and B-V-4) were from family B; two subjects (one male, C-III-2, and one female carrier, C-II-3) were from family C; and two subjects (one male, D-IV-3, and one female carrier, D-III-2) were from family D (Fig. 1).

Genetic Testing

Genetic testing was performed to identify mutations in the *CHM* gene. Genomic DNA was isolated from patient and control white blood cells according to standard methods and then PCR-amplified using previously described primer pairs.[29] Bidirectional sequencing of all 15 exons of the CHM gene and adjacent splice sites was performed and the resulting sequence data compared with the published sequence.

X-inactivation was assayed on two symptomatic female carriers with severe phenotypes (subjects B-V-3 and C-II-3) by restriction fragment length polymorphism analysis using a methylation sensitive enzyme, Hpa II, followed by PCR amplification of a $(CAG)_n$ triplet repeat region in the androgen receptor gene on the X chromosome. Methylation sensitive enzymes cut the androgen receptor repeat region

on the active X chromosome, but leave this site intact on the inactive X chromosome. The X-inactivation ratio is obtained by comparing quantitative PCR results with and without digestion by the methylation sensitive enzyme. A ratio of more than or equal to 90:10 is consistent with severe skewed X-inactivation.[30]

Clinical Examination

Best-corrected visual acuity (BCVA) was measured using a standard eye chart according to the Early Treatment of Diabetic Retinopathy Study (ETDRS) protocol. Goldmann kinetic perimetry was performed with V-4e and I-4e targets. Isopters were converted into retinal areas (mm²) and compared with the average V-4e and I-4e field areas for eight eyes of eight normal subjects aged 15 to 75 years (mean age $\pm$ SD = 41.1 $\pm$ 21.7); planar data were converted to solid visual field angles and retinal areas using previously published methods.[31] Pupils were dilated with 1% tropicamide and 2.5% phenylephrine prior to obtaining color fundus photographs using digital fundus cameras (Topcon 50EX and Topcon 50IX; Topcon Medical Systems, Oakland, NJ). SD-OCT and fundus autofluorescence (FAF) images were obtained (Spectralis HRA + OCT Laser Scanning Camera; Heidelberg Engineering, Vista, CA) in all members from families A, B, and D as previously described.[32] Briefly, the infrared beam of the super luminescent diode, center wavelength 870 nm, was used to acquire 20° horizontal scans through the locus of fixation; scans included 100 A-scans/B-scan for images through the locus of fixation, and 10 A-scans/B-scan for the 19 horizontal scans used to acquire the 20° × 15° volume scans. A macular SD-OCT image acquired with the Spectralis (top) and Bioptigen (bottom) system from a normal subject, aged 36 years, is shown in Supplementary Figure S1 (see Supplementary Material and Supplementary Fig. S1, http://www.iovs.org/lookup/suppl/doi:10.1167/iovs.12-10707/-/DCSupplemental) and the bands representing the outer retinal layers are numbered. Thirty-degree fundus autofluorescence images centered on the fovea were acquired by asking the subject to look at the central fixation target. High-resolution line scans were acquired from patients in family C (Bioptigen SD-OCT; Bioptigen, Inc., Research Triangle Park, NC) as previously described.[24] Full-field electroretinography (ffERG) was performed after 45 minutes of dark adaptation using Burian-Allen contact lens electrodes (Hansen Ophthalmic Development Laboratory, Iowa City, IA), according to the standards of the International Society for Clinical Electrophysiology and Vision (ISCEV)[33] and as described elsewhere.[23]

AOSLO Image Acquisition

High-resolution images were obtained using AOSLO at University of California, Berkeley (families A and B); University of California, San Francisco (families A and D); and the Medical College of Wisconsin (family C) as described previously.[34-36] Digital videos were recorded in real-time at various locations surrounding fixation. Distortions in images caused by eye movements were accounted for and corrected using registration algorithms as previously described.[37] In addition, subject C-III-2 underwent imaging with a flood illuminated AO imaging system, as previously described.[38] Fixed frames were averaged into an image that was then arranged (Adobe Photoshop; Adobe Systems Inc., Mountain View, CA) to create a continuous montage.

Cone Spacing Analysis

Cone spacing measures were determined using previously described methods[23] and compared with measures from 24 age-similar normal subjects. *Z*-scores, or standard deviations (SD) from the normal mean, were calculated for each cone spacing measurement. *Z*-scores greater than 2 were considered abnormal. In some locations with normal *Z*-scores, the 2D Fourier spectrum was analyzed using custom numerical computing software (MATLAB; MathWorks, Natick, MA). The power spectra show an elliptical ring, whose mean radius corresponds to the spatial frequency of the cone mosaic (or the inverse of the mean row-
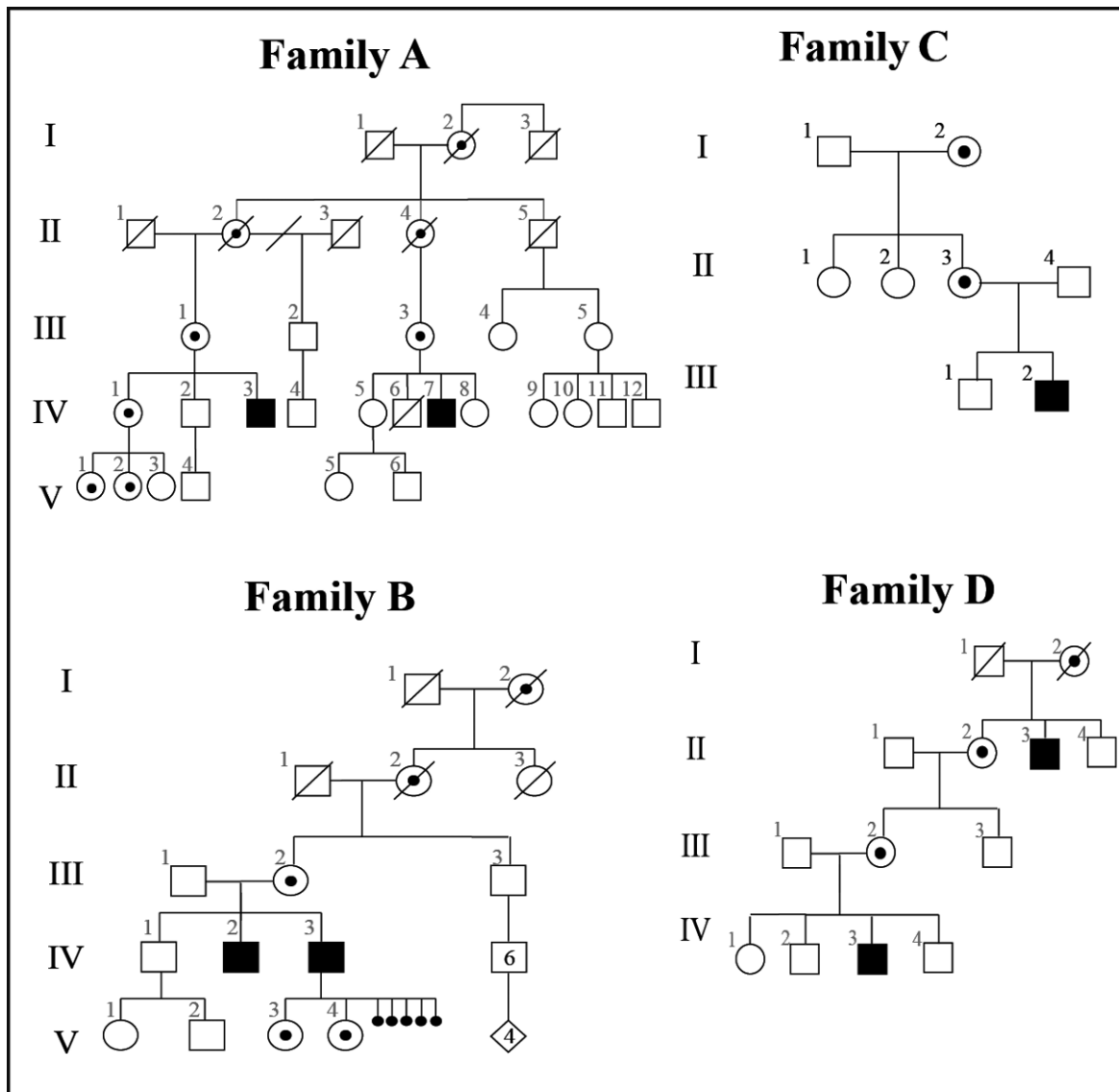
FIGURE 1. Pedigrees for the 4 families with choroideremia. *Squares*: males. *Circles*: females. *Diamond*: sex unknown. *Filled symbols*: males with CHM. *Circles with dark centers*: female carriers. *Small filled circles*: spontaneous abortions (sex unknown). *Diagonal line*: deceased. Transmission was consistent with X-linked inheritance in each family and the four families were unrelated.

to-row cone spacing) at a given retinal location.[23,39,40] Cone spacing measures obtained by this method were compared with cone spacing measures obtained by previously described methods[23] at selected retinal locations to determine if rods were included in quantitative measures of cone spacing at locations with normal *Z*-scores.

RESULTS

Genetic Testing

Molecular analysis identified a deletion of exons 9 to 15 in family A; a splice site mutation (G to A) at position 79+1 of exon 1 in family B; a deletion of exons 6 to 8 in family C; and a nucleotide substitution resulting in an amino acid change of Gln106Stop in family D. The symptomatic carriers with the most severely abnormal phenotypes, B-V-3 and C-II-3, were found to have a severe skewed X-inactivation pattern (100:0).

Clinical Examination

Clinical characteristics of all subjects are summarized in Table 1. The subjects ranged in age from 14 to 70 years (mean 39 years, SD 20 years). BCVA ranged from 20/16 to 20/20 in asymptomatic carriers, from 20/20 to 20/63 in symptomatic carriers, and from 20/25 to 5/63 in affected males. Visual field results are described in Table 2. Fundus examination in the asymptomatic carriers (Fig. 2, subjects A-V-2 and D-III-2) showed hypopigmented patches that correlated with areas of hypoautofluorescence (yellow circles, Fig. 2). A heterogeneous pattern of autofluorescence was present throughout the fundus in all carriers (Fig. 2). Horizontal SD-OCT scans through fixation showed attenuation of band 3 underlying a normal band 2 in a region of reduced autofluorescence (blue squares, Fig. 2). Band 3 became attenuated or disappeared completely in the presence of an intact band 2 peripheral to the region highlighted by yellow arrows in all carriers but two (Fig. 2,

TABLE 1. Summary of Clinical and Molecular Characteristics of Choroideremia Subjects Studied

Patient Number/Sex	Age at Visit, y	Symptom Duration, y	CHM Genetic Change	Exons	BCVA OD, OS	ETDRS Score OD, OS	Foveal Sensitivity (dB) OD, OS	ffERG Photopic 30 Hz Flicker Amplitude (μV), Timing (ms)*; OD, OS	AOSLO Imaging, Eye
A-III-1/F	70	30	Heterozygous deletion	9-15	20/25, 20/63	80, 63	33, 19	82, 28.7; 68, 29.2	OD
A-IV-3/M	44	24	Hemizygous deletion	9-15	20/25, 20/160	83, 45	37, NP	3.2, 38; 3.4, 37.9	OD
A-V-2/F	26	No symptoms	Not tested	Not tested	20/16, 20/20	88, 85	36, 38	138.5, 26; 139.6, 26	OU
B-IV-2/M	66	57	Hemizygous G/A splice site mutation position 79+1	1	20/32, 20/50	NP	30, <0	NP	NP
B-IV-3/M	63	30	Hemizygous G/A splice site mutation position 79+1	1	20/50, 5/63	67, 28	NP	NP	NP
B-V-3/F	25	13	Heterozygous G/A splice site mutation position 79+1	1	20/20, 20/20	85, 85	36, 36	18.8, 36.4; 15.3, 35.2	OU
B-V-4/F	22	2	Heterozygous G/A splice site mutation position 79+1	1	20/20, 20/20	85, 85	NP	NP	NP
C-II-3/F	47	1	Heterozygous deletion	6, 7, 8	20/20, 20/40	NP	36, 33	Nonmeasurable	OD
C-III-2/M	14	2	Hemizygous deletion	6, 7, 8	20/40, 20/100	NP	38, 35	34.7, 34; 32.5, 34.5	OD
D-III-2/F	38	No symptoms	Heterozygous CAG > TAG nucleotide substitution; Gln106Stop		20/16, 20/20	88, 85	36, 36	138.5, 28; 135.7, 28	OU
D-IV-3/M	16	4	Hemizygous CAG > TAG nucleotide substitution; Gln106Stop		20/25, 20/25	78, 80	35, 34	9.8, 41; 9.3, 38	OU

NP, not performed; ETDRS, early treatment of diabetic retinopathy visual acuity score, expressed as number of letters correctly identified.
* Normal mean ffERG photopic 30 Hz flicker amplitudes = 121 μV; 2 SD below normal is 56 μV; normal photopic 30 Hz flicker timing is <32 ms.

subjects A-III-1 and B-V-3) in whom band 3 was indistinct throughout the macula. In addition, SD-OCT scans showed bridging hyperreflective structures or interlaminar bridges[21] (A-III-1, Fig. 2C, bottom rows, red arrows) as also observed in male patients (C-III-2 and A-IV-3, Figs. 3A, 3C, bottom rows, red arrows).

Fundus findings in the symptomatic carriers (Fig. 2, subjects A-III-1, B-V-3, and C-II-3) revealed RPE and choroidal atrophy around the optic nerve and the temporal arcades, with involvement of the central macula in one carrier (A-III-1) who had a discrete region of atrophy inferior to the fovea (Fig. 2). FAF in these carriers showed reduced autofluorescence in areas of RPE atrophy and mottled hyperautofluorescence interspersed with hypoautofluoresence elsewhere (Fig. 2).

Fundus examination in affected males revealed RPE and choroidal atrophy that did not involve the fovea in the eyes imaged (Fig. 3), although foveal atrophy was present in the worse eye of subjects A-IV-3, B-IV-2, and C-III-2 (Table 1, images not shown). FAF in the youngest patient (Fig. 3, C-III-2) showed a heterogeneous pattern of autofluorescence similar to the symptomatic carriers in the macula (Fig. 2) with RPE atrophy extending within the temporal arcades. The SD-OCT scan through fixation (Fig. 3A, C-III-2, bottom) showed attenuation of band 3 (Fig. 3A, bottom, left of black arrow), and then band 4a (yellow arrow), with loss of bands 3 and 4a in the presence of an attenuated band 2 at greater eccentricities (Fig. 3A, bottom, blue arrow). The region between the black and yellow arrows appears to show greater attenuation of the intensity of band 3 compared with band 4.

Round, hyperreflective structures were present in the outer retina in three male patients (D-IV-3, A-IV-3, and B-IV-2, aged 16, 44, and 66 years, respectively; black asterisks on Fig. 3) and two symptomatic carriers (B-V-3 and A-III-1, aged 25 and 71 years, respectively; not shown). These outer retinal tubulations[43] (ORT) were seen in areas of RPE atrophy where FAF was severely reduced. The affected males (D-IV-3, A-IV-3, and B-IV-2) also showed hyporeflective cavities consistent with inner retinal microcysts[44] with associated loss of the outer nuclear layer (Figs. 3B–D, bottom rows), and bridging hyperreflective structures or interlaminar bridges[21] (C-III-2 and A-IV-3, Figs. 3A, 3C, bottom, red arrows).

Electroretinography

ffERG showed normal rod and cone responses in three carriers, while in two symptomatic carriers (B-V-3 and C-II-3), the rod and cone responses were severely reduced (Table 1). Rod responses were not measureable and cone responses were severely reduced but measureable to a 30-Hz flicker stimulus in all three male patients tested; ERG testing was not performed on the 2 most severely affected male patients (B-IV-2 and B-IV-3), but waveforms had been unrecordable in the past.

High-Resolution Imaging with AOSLO

Cone mosaics appeared normal and cone spacing measures were within normal limits in the central macula in the asymptomatic carriers (A-V-2 and D-III-2, not shown). Cone coverage was less contiguous compared with normal and cone spacing did not follow typical changes with retinal eccentricity in symptomatic carriers (Figs. 4A, 4B). Symptomatic carriers showed patchy areas where cone spacing was increased interspersed with areas of normal cone spacing in central regions with preserved RPE (Figs. 4A, 4B). In carrier C-II-3, cone mosaics were normal where bands 2, 3,

TABLE 2. Summary of Visual Field Tests

Patient Number/Sex	Age at Visit, y	Eye	Automated Perimetry (Humphrey Visual Field 10-2)	Kinetic Perimetry (Goldmann Visual Field)	Preserved I-4e and V-4e Visual Field Areas*	
					V4e	I4e
A-III-1/F	70	OD	6° superotemporal scotoma	V4e: full; I4e: constricted	100%	87.4%
		OS	Dense 20° scotoma in the inferior hemisphere	V4e: 10° central scotoma; I4e: 25° cecocentral scotoma	82.4%	63.3%
A-IV-3/M	44	OD	Constricted to central 9°	V4e: central 10° island with preserved 120° inferior island; I4e: central 10° island	32.7%	1.5%
		OS	NP	V4e: central 25° island with preserved 20° peripheral ring; I4e: central 3° island	20.5%	0.4%
A-V-2/F	26	OD	Full fields	V4e: full; I4e: full	99.3%	100%
		OS	Full fields	V4e: full; I4e: full	100%	100%
B-IV-2/M	66	OD	Constricted to central 9°	NP	NP	NP
		OS	Constricted to 9° in the inferonasal quadrant with inferonasal fixation	NP	NP	NP
B-IV-3/M	63	OD	NP	V4e: 90° ring scotoma; I4e: central 5° island	40.9%	0.5%
		OS	NP	V4e: central 5° island, preserved inferior ring from 135-30°; I4e: not perceived	33.3%	0%
B-V-3/F	25	OD	Full fields	V4e: constricted; I4e: central 20° island	52.7%	4.5%
		OS	3° inferotemporal scotoma	V4e: 15° incomplete ring scotoma; I4e: central 15° island	43.8%	3.8%
B-V-4/F	22	OD	NP	V4e: full; I4e: full	100%	100%
		OS	NP	V4e: full; I4e: full	100%	100%
C-II-3/F	47	OD	Constricted to central 9°	V4e: 20° paracentral scotomas; I4e: constricted	65%	24.2%
		OS	Constricted to central 9°	V4e: temporal 20° scotomas; I4e: constricted	78.9%	14.5%
C-III-2/M	14	OD	Constricted to central 9°	V4e: 30° paracentral scotomas; I4e: constricted	89.6%	8.4%
		OS	Constricted to central 9°	V4e: 30° paracentral scotomas; I4e: constricted	95.8%	28%
D-III-2/F	38	OD	Full fields†	V4e: full; I4e: full	96.1%	94.5%
		OS	Full fields†	V4e: full; I4e: full	92.1%	91.7%
D-IV-3/M	16	OD	Constricted to central 15°	V4e: constricted; I4e: central 5° island	81.0%	1.3%
		OS	Constricted to central 15°	V4e: constricted; I4e: central 5° island	85.8%	1.1%

* Preserved visual field expressed as percentage of average field area for eight normal subjects aged 15 to 75 years (mean age $\pm$ SD = 41.1 $\pm$ 21.7), values equal or greater to 100% of normal are reported as 100%. Normal limits for visual field area to the V4e target (mean $\pm$ 2 SD) = 666.6 to 838.1 mm^2 and for the I4e target = 494.1 to 708.2 mm^2.

† Humphrey visual field 30-2 results are presented for these subjects.

and 4 were intact near the fovea (Fig. 4, black arrow, inset A2), but disrupted with increased cone spacing overlying areas of band 3 attenuation 3 to 4 degrees peripheral to the fovea, in regions where band 2 was intact (Fig. 4A, insets A1 and A3). Regions of increased cone spacing were interspersed with regions where cone spacing was normal; however, cones near the edge of the montage with normal Z-scores did not appear normal and were sometimes associated with regions where band 2 was irregular and band 3 was absent (Fig. 4B, inset B3). This pattern is consistent with a mosaic pattern of retinal cone and RPE loss as has been reported in choroideremia carriers.[3,15,16,45,46]

Cone spacing in males with CHM showed two patterns of cone loss. In the first pattern, cone spacing was normal near the fovea (Fig. 4C, inset C2) but cone mosaics were disrupted peripherally where quantitative measures of cone spacing were not possible (Fig. 4C, inset C1). At this location, band 3 was attenuated in comparison with bands 2 and 4, as was also

observed in Figure 3A. The second pattern was observed in patients A-IV-3 and D-IV-3, who showed increased cone spacing near the fovea, but normal cone spacing Z-scores near the edges of regions where cones could be visualized in regions where bands 2 and 3 were irregular or disrupted (Fig. 4D, insets D2 and D1). To assess for the possible inclusion of rods in cone spacing measures, a Fourier spectrum analysis of AOSLO images at locations 2 to 4 degrees from the fovea with normal Z-scores showed similar results to cone spacing obtained by manual cone selection, excluding the possibility of the erroneous inclusion of rods in measures of cone spacing.

Flood-illuminated AO images at the fovea in patient C-III-2 revealed a complete contiguous cone mosaic with numerous round, low frequency structures that were not visible in AOSLO images (Fig. 5). Such structures have not been observed in flood-illuminated AO images of normal eyes or other eyes with CHM. We measured the center-to-center spacing of these structures using previously described methods[47] and found the

A-V-2, 26 yrs/F
VA 20/16 OD, 20/20 OS

D-III-2, 38/F
VA 20/16 OD, 20/20 OS

A-III-1, 70 yrs/F
VA 20/25 OD, 20/63 OS

B-V-3, 25 yrs/F
VA 20/20 OS, 20/20 OD

C-II-3, 47 yrs/F
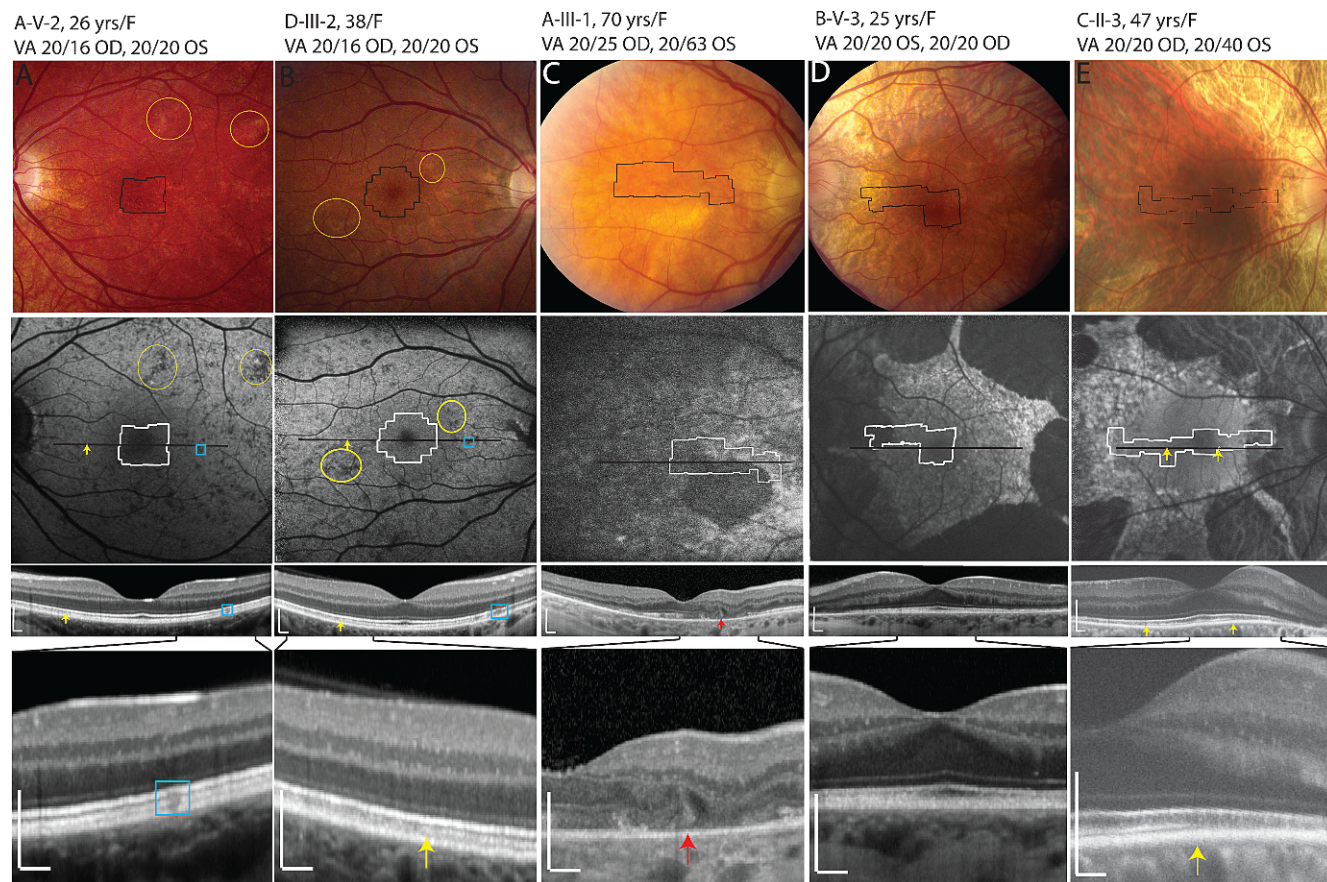VA 20/20 OD, 20/40 OS

FIGURE 2. Color fundus photo (*top*), FAF (*middle*), and SD-OCT images (*bottom two rows*) in female CHM carriers. *Outlines on color fundus photo and FAF images*: location of AOSLO images. *Black lines*: horizontal SD-OCT scan locations; the span of the lower magnified SD-OCT scans is indicated by the *solid black lines* coming from the images above them. *Yellow ellipses*: examples of hypopigmentation on color fundus photo that correlate with hypoautofluorescence on FAF. *Blue squares*: areas of hypoautofluorescence that correlate with areas of attenuated SD-OCT bands 3, 4a, and 4b; *yellow arrows* indicate the border at which band 3 becomes attenuated or disappears completely. In (**D**) (B-V-3), bands 3 and 4 were attenuated throughout the macula. *Red arrow*: bridging hyperreflective structures or interlaminar bridge seen in A-III-1.[21] All OCT images were acquired using the Spectralis system with the exception of C-II-3, whose images were acquired with the Bioptigen system. *White horizontal* and *vertical scale bars* on the SD-OCT images indicate 200 μm.

DISCUSSION

mean spacing was 12.29 μm (95% confidence interval: 12.23–12.34 μm). The number of cones per low frequency structure ranged from approximately 10 to 20.

DISCUSSION

The pathogenetic mechanism underlying retinal degeneration in choroideremia is not clearly understood, but may be due to a deficiency in the prenylation of multiple Rab proteins.[48] Some histological reports of eyes with advanced CHM have shown lack of OS phagocytosis by the RPE,[19] while others suggested secondary loss of RPE and photoreceptors caused by choroidal atrophy.[20] The eyes from a 30-year-old man with CHM showed independent degeneration of the choriocapillaris, RPE, and photoreceptors, but also reported significantly better visual function than would be predicted by the retained RPE and choriocapillaris, perhaps suggesting that RPE or choroidal atrophy precedes photoreceptor degeneration.[14] While some OCT studies of CHM patients show early photoreceptor IS/OS and ONL degeneration in the presence of normal[21] or attenuated RPE,[49] others demonstrate preservation of the ONL and OS in areas with attenuated or absent RPE.[50] Based on histological studies of female carriers, authors have concluded that the primary defect was at the level of RPE,[15] rod

photoreceptors,[16] or the retina, RPE, and choroid simultaneously.[45]

Given the lack of clarity regarding the initial site of disease in the published literature, we examined retinal structure at high resolution in living eyes with CHM in an effort to shed light on the pathogenesis of this disease. We observed characteristic FAF findings in all carriers similar to the pattern reported in animal models[6] and in prior studies of human CHM carriers.[51] It has been proposed that the observed hyperautofluorescence results from rod loss; the outer segments of degenerating rods are digested by the RPE, causing increased lipofuscin accumulation and hyperautofluorescence.[6] Hypoautofluorescence, in contrast, occurs secondary to loss of RPE cells and thinning of the RPE layer.[6] Patches of hypoautofluoresence in the two asymptomatic carriers who had normal ERG findings and full visual fields correlated with patches of hypopigmentation throughout the fundus. Prior work has reported fundus hypopigmentation, RPE mottling, and reduced dark-adapted ERGs as the first manifestations of complete deletion of the *CHM* gene in a 4-year-old boy, with dark-adapted cone sensitivity abnormalities in his obligate carrier mother.[50] Since our asymptomatic carriers had normal dark-adapted ERGs but showed hypopigmented fundus findings and attenuation of band 3 on SD-OCT that correlated with areas of hypoautofluoresence, degeneration of the contact cylinder
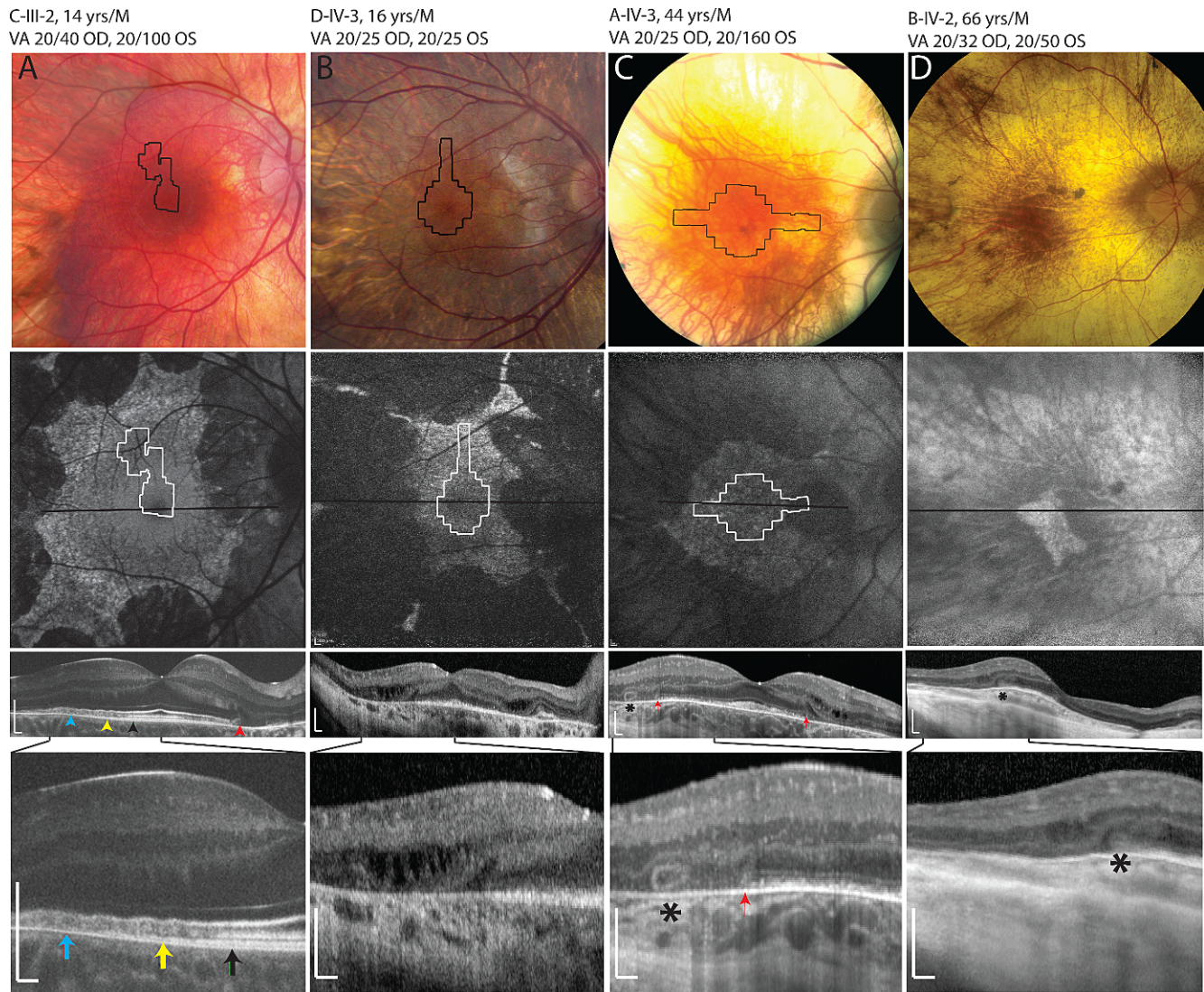
C-III-2, 14 yrs/M
VA 20/40 OD, 20/100 OS

D-IV-3, 16 yrs/M
VA 20/25 OD, 20/25 OS

A-IV-3, 44 yrs/M
VA 20/25 OD, 20/160 OS

B-IV-2, 66 yrs/M
VA 20/32 OD, 20/50 OS

FIGURE 3. Color fundus photo (*top*), FAF (*middle*), and SD-OCT images in male CHM patients. In the most severely affected patient (B-IV-2, [**D**]), AOSLO images did not reveal unambiguous cone mosaics, although an island of hyperautofluorescent RPE and outer retinal structures was present at the fovea; the SD-OCT scans in this patient demonstrate outer retinal tubulations (*asterisk*) and inner retinal microcysts. *Outlines on color fundus photo and FAF images*: locations of AOSLO images. *Black lines*: horizontal SDOCT scan locations; the span of the lower magnified SDOCT scans is indicated by the *solid black lines* coming from the images above them. *Black asterisks*: outer retinal tabulations. *Red arrows*: interlaminar bridges. *Black arrow*: edge of region where all outer retinal bands are present. *Yellow arrow*: intact band 2, but attenuated band 3. *Blue arrow*: only bands 1, 2, and 4 are visualized. All OCT images were acquired using the Spectralis system with the exception of C-III-2, whose images were acquired with the Bioptigen system. *White horizontal* and *vertical scale bars* on the SD-OCT images indicate 200 μm.

between the RPE apical processes and the external portion of the cone outer segments, possibly including the cone outer segment tips,[42] may be the first manifestation of CHM in these carriers.

Although AOSLO images were not acquired in areas of abnormal autofluorescence, we observed abnormal cone structure in areas where the band 3 was disrupted in the presence of an intact band 2 on SD-OCT. In the present study all subjects except for two carriers and one affected male with early disease showed attenuation of band 3 with an overlying intact band 2. Others have interpreted this finding to indicate that RPE cells degenerate prior to photoreceptor degeneration; CHM eyes showed abnormally thin RPE underlying normal OS and ONL layers, in contrast to the pattern seen in patients with RP, where thinning occurs first in the OS, then in the ONL with

relative preservation of the RPE.[49] These observations may suggest that the RPE is the primary layer affected by CHM.

However, some studies have defined the fourth outer retinal band as follows: As illustrated in Supplementary Figure S1 (see Supplementary Material and Supplementary Fig. S1, http://www.iovs.org/lookup/suppl/doi:10.1167/iovs.12-10707/-/DCSupplemental), band 4a represents a combination of rod outer segment tips and apical RPE, and 4b corresponds to the region of basal RPE and Bruch's membrane, at extrafoveal locations.[41] In our images of CHM patients, the delineation between sublayers 4a and 4b was ambiguous in most scans, but was more evident in scans acquired using the Bioptigen system (see Supplementary Material and Supplementary Fig. S1, http://www.iovs.org/lookup/suppl/doi:10.1167/iovs.12-10707/-/DCSupplemental, bottom panels; Figs. 3A, 4A, 4C). In Figures 3A, 4A, and 4C, regions of degeneration
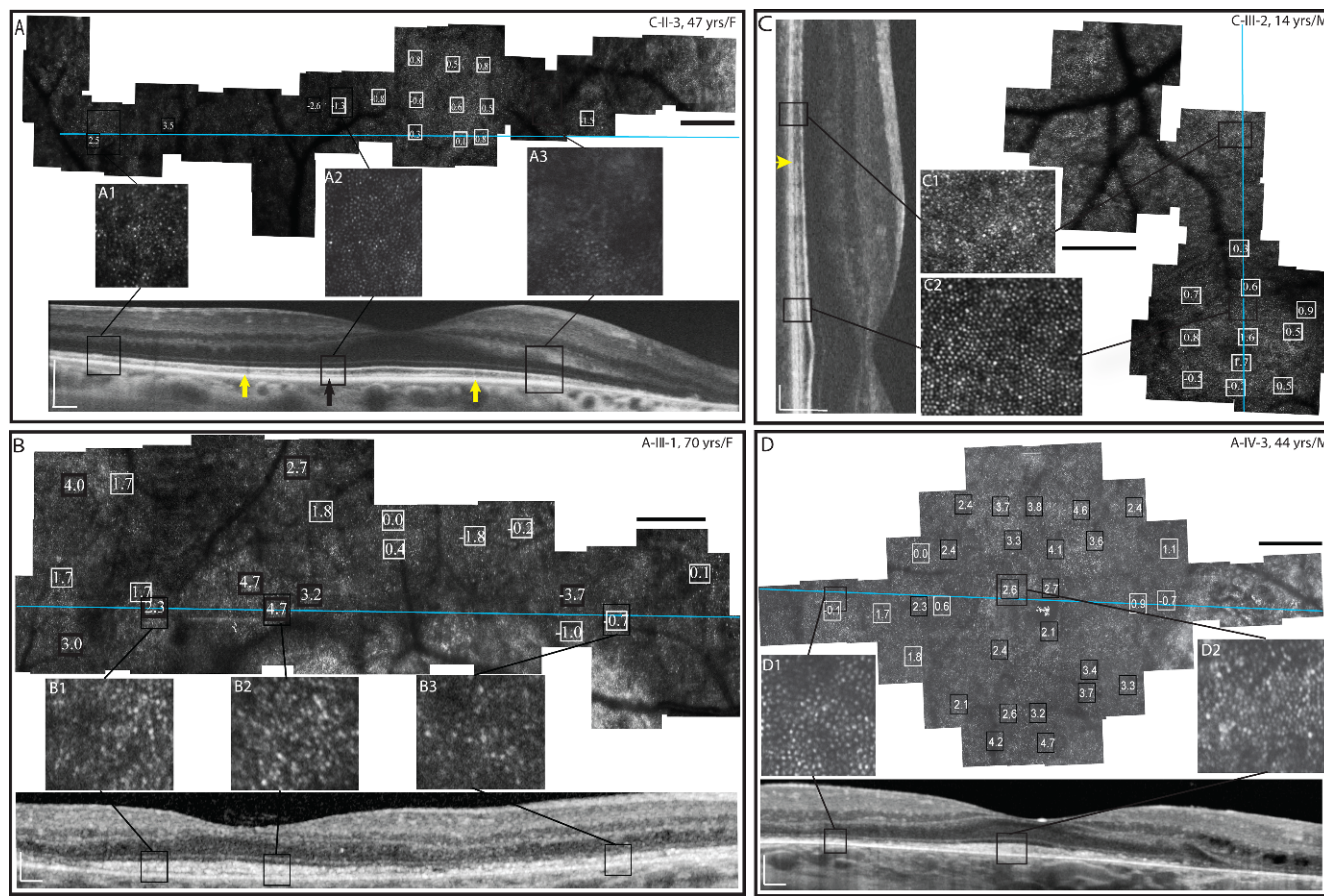
FIGURE 4. High-resolution AOSLO images for two carriers (*left panels*) and two affected males with CHM (*right panels*). *Blue line*: SD-OCT scan location. *White boxes*: cone spacing Z-scores within 2 SD of the normal mean. *Black boxes*: cone spacing Z-scores greater than 2 SD of the normal mean. *Black arrow*: area where bands 2, 3, and 4 are intact (magnified AOSLO, *inset* [**A2**]). *Yellow arrows*: area where bands 3 and 4 are attenuated but band 2 is intact; *black scale bar*: 1°. *Large black squares* show locations of magnified AOSLO insets; (**A1**, **B1**) show increased cone spacing in regions with disruption of band 3 but preservation of band 2; (**A2**, **B2**) show normal cone spacing in regions with intact outer retinal bands; (**A3**) shows a region where unambiguous cones were not visible and cone spacing measures were not possible with band 3 loss and band 2 preservation, and (**B3**) shows a region where cone spacing Z-scores were normal but the cones appeared abnormal with irregular packing; band 2 is irregular and band 3 is absent. (**C2**) shows normal cone spacing and an intact mosaic with intact outer retinal bands, while (**C1**) shows disrupted cones that were not arranged in mosaics, precluding quantitative measurement of cone spacing, in a region where band 2 is preserved but band 3 is attenuated or absent. *Inset* (**D2**) shows increased cone spacing near the fovea in a region where band 2 is intact but band 3 is irregular, while *inset* (**D1**) highlights an area at the edge of atrophy where cone mosaics appear abnormal although cone spacing is within 2 SD of the normal mean, band 2 is attenuated and band 3 is absent. All OCT images were acquired using the Spectralis system with the exception of (**A**, **C**), showing images from C-II-3 and C-III-2, whose images were acquired with the Bioptigen. *White horizontal* and *vertical scale bars* on the SD-OCT images indicate 200 μm.

showed preservation of band 2 in the absence of band 3 with preservation of band 4, perhaps indicating degeneration of the interface between cone outer segments and apical RPE processes. Regions with loss of band 3 in the presence of preserved bands 2 and 4 may represent selective cone photoreceptor outer segment damage in regions with intact RPE cells, which would be perfectly consistent with the apparently normal RPE autofluorescence at those regions as shown in Figure 3A.

However, AOSLO images at regions where the band 3 was attenuated but band 2 was intact showed disrupted cone photoreceptors in an affected male (Fig. 4, insets D2 and C1) and increased cone spacing in two symptomatic carriers (Fig. 4, insets A1, A3, and B1). This finding suggests cone photoreceptors were abnormal in areas with disruption of the contact cylinder between the RPE apical processes and the cone outer segment tips, in the presence of preserved inner segment ellipsoid (ISe) bands on SD-OCT.[42] High-resolution images of the cone photoreceptor mosaic may provide insight into the relationship between photoreceptor and RPE cell

death, and suggest that the contact cylinder between the RPE apical processes and the cone photoreceptor outer segments degenerates even in the presence of an apparently intact ISe band observed on SD-OCT. The attenuation or loss of this layer could be due to loss of the RPE apical processes, the cone photoreceptor outer segments, or the interface between these structures.

The SD-OCT bands 4a and 4b are complex and represent interdigitations between rod and cone outer segments and the apical microvilli of the RPE,[41] which are not well resolved or discriminated using standard, commercially available SD-OCT systems including the systems used in the present manuscript. It is possible that higher resolution OCT systems,[52] such as adaptive optics OCT,[53,54] could distinguish between cone and rod outer segment tip loss and RPE damage. Since disruption or loss of the OS/RPE, cone outer segment tip, and rod outer segment tip bands may represent primary degeneration of photoreceptors or simultaneous photoreceptor and RPE cell degeneration, the ambiguity in our images highlights areas for future investigation using AO-
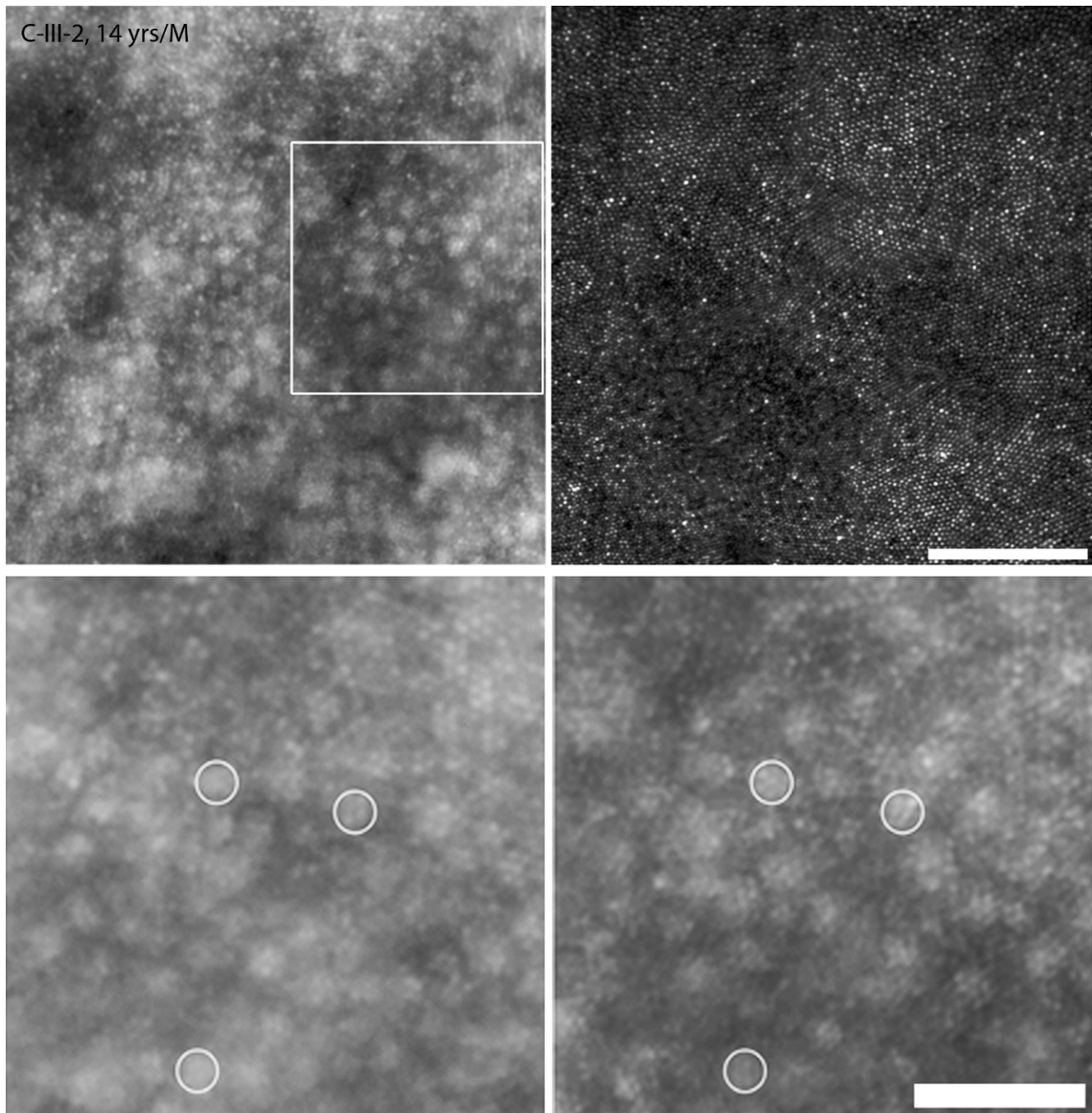
FIGURE 5. Low-frequency structures observed in AO images at the fovea in a CHM patient, C-III-2. *Top panels*: comparison of foveal montages from flood illuminated AO and AOSLO images. The flood-illuminated AO image (*left*) shows low-frequency structures, not visible on AOSLO images (*right*) which show cone photoreceptors. *White scale bar*: 100 μm. *Bottom panels*, magnified images of the region delimited by the *white box* in the *left-upper panel* show a comparison of AO flood images of the fovea in the same patient over 6 months; the low-frequency structures remain stable. *White circles*: three corresponding retinal locations. *White scale bar*: 50 μm.

OCT to probe these interfaces in choroideremia patients, which may provide additional insight into the primary site of degeneration in choroideremia.

In other male patients, areas of normal cone spacing were seen 2 to 4 degrees peripheral to the fovea while cone spacing was increased near the fovea. Unlike patients with primary cone degeneration, in which central cone spacing is increased even in early stages—or retinitis pigmentosa (RP), in which cones are well-preserved centrally but become increasingly sparse with eccentricity at the edges of scotomas[23]—the present manuscript demonstrates abnormal cones at the fovea in affected males with CHM, while cone spacing Z-scores were more normal at the edges of the preserved retinal regions (Figs. 4C, 4D). Possible explanations for this finding include the following. First, cone spacing may appear more normal at the edge of degeneration because the imaging properties of degenerating cones change. The degenerating photoreceptors were observed to

form ORT, which have been reported in imaging studies of CHM,[43,44] gyrate atrophy,[55] Bietti crystalline retinopathy,[43,56] retinal degeneration associated with a mitochondrial DNA mutation (A3242G), central serous retinopathy, age-related macular degeneration, and other diseases such as pattern dystrophy associated with choroidal neovascularization.[43] ORT typically occur in areas with disruption of outer retinal architecture and relative preservation of the photoreceptor layer with preserved ISe bands, often overlying RPE damage or at the margin between preserved and absent RPE and photoreceptor layers.[43] Zweifel and colleagues have proposed that ORT may represent a final common pathway in a variety of retinal degenerative conditions that are initiated by loss of interdigitation of the outer segments with RPE or degeneration of the RPE, followed by disruption of attachment to neighboring neural elements such as Müller cells with outward folding of the photoreceptor layer until opposite sides of the fold establish contact and form new lateral connections, reconstituting the IS/OS junction and forming a tubular structure.[43] The occurrence of ORT in CHM may indicate primary degeneration of RPE cells with secondary effects on photoreceptors, and may affect cone spacing measures as the outer retina forms tubules adjacent to regions of atrophy. In addition, the interlaminar bridges first reported by Jacobson and colleagues[21] may contribute to ORT formation, and similarly may affect the imaging properties of cones near the advancing margins of degeneration. The interlaminar bridges have been attributed to hyperplastic Müller cells in response to retinal degeneration, with altered optical properties that affect their imaging characteristics[21]; a similar phenomenon may account for the apparent decreases in cone spacing observed in the present manuscript at the edges of degeneration. Second, cones may be more abnormal at the fovea than at the edge of atrophy. This is unlikely for 2 reasons: first, automated perimetry showed foveal sensitivity was better preserved, while sensitivity was more abnormal at retinal locations with increased eccentricity; and second, SDOCT images showed that the outer retinal layers were better preserved near the fovea than in extrafoveal locations; but it is possible that the cones are structurally more intact, although less normal functionally, at the margins of degeneration. Even if cone spacing is more normal at the peripheral edges of the AOSLO montages, the cones at the margins of degeneration are likely not normal; cones in these regions appeared crenelated and shrunken in comparison with normal cone mosaics (Fig. 4, insets A3, B3, C1, and D1). Third, rods may be present at the edge of atrophy. Since rods are smaller than cones, quantitative measures of photoreceptor spacing that include rods will produce a lower mean spacing than ones that include only cones. However, cone spacing measures by Fourier spectrum analysis of AOSLO images showed similar results to cone spacing obtained by manually selecting cones, suggesting rods were not included in our manual cone spacing measures.

In primary photoreceptor degenerations such as RP, cones are better preserved at the fovea and cone spacing increases near the edge of the remaining photoreceptor mosaic, beyond which RPE cell mosaics may be seen.[23] RPE mosaics were not observed peripherally in the CHM patients in this study, perhaps because RPE cells degenerate primarily or simultaneously with photoreceptors. Alternatively, CHM may affect the imaging properties of RPE cells, which may require normal melanin content and distribution to be visualized; RPE cells in CHM carriers have abnormal melanin granule distribution[16] and lack basal microvilli and infoldings.[45]

The present manuscript also demonstrates distinct information that can be acquired using different AO imaging modalities (AOSLO and flood-illuminated AO). At the fovea of a young CHM patient with well-preserved visual acuity and cone spacing, we observed low-frequency structures simultaneously with overlying cones using an AO flood-illuminated system. The low-frequency structures were consistent in size with RPE cells at the location imaged, and were associated with a similar number of overlying photoreceptors as have been associated with RPE cells in histological studies.[57-61] Gao and Hollyfield[59] reported RPE cell center-to-center spacing ranging from 12.45 μm at the fovea to 13.87 μm at 120 μm from the foveal center, and reported a density of 22 cones/RPE cell at the fovea; Watzke and associates reported center-to-center spacing of 14 μm within 250 um of the foveal center,[61] and Dorey and associates reported RPE cell sizes of 10.12 μm[58]; however, these measures from histological studies of excised human ocular tissues may reflect artifact introduced by histological processing. Roorda and colleagues observed RPE cells directly in AOSLO images after extensive cone photoreceptor loss with cell spacing of 14.85 to 15.2 μm in locations ranging from 100 to 750 μm.[47] Morgan and colleagues[62] reported RPE cell nearest neighbor distances ranging from 10.8+/−1.7 μm at 5 degrees superior to the fovea using AOSLO autofluorescence imaging in normal humans, but no locations comparable with those in the present image were studied. The low-frequency structures in the present study measured 12.23 μm at a distance of 130 μm from the fovea, which is comparable in size with other reports. The structures observed in the present study have not been observed with the same imaging system in normal eyes or other eyes with retinal degeneration, and were not visible on the AOSLO image of the same location due to confocality of the SLO system; light not originating from the focal plane of the retina was excluded through the use of a pinhole conjugate to the retinal focal plane, thus increasing the contrast of the final image.[63] However, scattered light from the fundus that comes from the RPE is usually masked by the light that comes from the overlying photoreceptor mosaic, and therefore, it is unusual to visualize RPE cells at a region where cone mosaics are intact.[47]

The findings in Figure 5 suggest that RPE cells are more visible in CHM patients than in normal eyes when imaged using flood illuminated adaptive optics systems with a near-infrared light source. The mechanism for this enhanced visibility may be due to abnormalities of melanin deposition in RPE cells with mutations in the *CHM* gene. Alternatively, enhanced RPE cell visibility could be due to selective abnormalities at the level of cone inner segments which cause a relative reduction of waveguided light originating from the cones without reducing backscattered light originating from the RPE.

In summary, high-resolution retinal imaging demonstrated abnormalities of FAF, retinal layer morphology, and cone morphology and spacing in CHM patients and carriers with a spectrum of clinical characteristics. Our high-resolution images of cone structure demonstrate a pattern of photoreceptor degeneration with ORT, microcystic inner retinal edema, and cone loss at the fovea with smaller, atrophic-appearing cones at the edge of degeneration which has not been observed in patients with primary photoreceptor degenerations.[23,32] Cone abnormalities in regions where SD-OCT band 3 showed attenuation in regions in which band 2 was intact suggest early involvement of RPE cells, likely in association with simultaneous photoreceptor cell degeneration because cone spacing was abnormal in many regions in which band 2 was intact. Longitudinal studies using high-resolution retinal imaging techniques may provide further insight into the ways cones and RPE cells are affected by *CHM* mutations. Furthermore, in vivo surrogate markers of photoreceptor structure such as those presented in the current manuscript should prove useful in evaluating the safety and efficacy of

experimental therapies for CHM, including gene replacement trials which are underway.

References

1. Coussa RG, Traboulsi EI. Choroideremia: a review of general findings and pathogenesis. *Ophthalmic Genet*. 2012;33:57–65.

2. Lyon MF. Gene action in the X-chromosome of the mouse (Mus musculus L.). *Nature*. 1961;190:372–373.

3. Vajaranant TS, Fishman GA, Szlyk JP, Grant-Jordan P, Lindeman M, Seiple W. Detection of mosaic retinal dysfunction in choroideremia carriers electroretinographic and psychophysical testing. *Ophthalmology*. 2008;115:723–729.

4. Cremers FP, Sankila EM, Brunsmann F, et al. Deletions in patients with classical choroideremia vary in size from 45 kb to several megabases. *Am J Hum Genet*. 1990;47:622–628.

5. Krock BL, Bilotta J, Perkins BD. Noncell-autonomous photoreceptor degeneration in a zebrafish model of choroideremia. *Proc Natl Acad Sci U S A*. 2007;104:4600–4605.

6. Tolmachova T, Anders R, Abrink M, et al. Independent degeneration of photoreceptors and retinal pigment epithelium in conditional knockout mouse models of choroideremia. *J Clin Invest*. 2006;116:386–394.

7. Duncan JL, Aleman TS, Gardner LM, et al. Macular pigment and lutein supplementation in choroideremia. *Exp Eye Res*. 2002;74:371–381.

8. MacDonald IM, Sauve Y, Sieving PA. Preventing blindness in retinal disease: ciliary neurotrophic factor intraocular implants. *Can J Ophthalmol*. 2007;42:399–402.

9. Preising M, Ayuso C. Rab escort protein 1 (REP1) in intracellular traffic: a functional and pathophysiological overview. *Ophthalmic Genet*. 2004;25:101–110.

10. Seabra MC, Brown MS, Slaughter CA, Sudhof TC, Goldstein JL. Purification of component A of Rab geranylgeranyl transferase: possible identity with the choroideremia gene product. *Cell*. 1992;70:1049–1057.

11. Sankila EM, Tolvanen R, van den Hurk JA, Cremers FP, de la Chapelle A. Aberrant splicing of the CHM gene is a significant cause of choroideremia. *Nat Genet*. 1992;1:109–113.

12. van den Hurk JA, van de Pol TJ, Molloy CM, et al. Detection and characterization of point mutations in the choroideremia candidate gene by PCR-SSCP analysis and direct DNA sequencing. *Am J Hum Genet*. 1992;50:1195–1202.

13. Cremers FP, Armstrong SA, Seabra MC, Brown MS, Goldstein JL. REP-2, a Rab escort protein encoded by the choroideremia-like gene. *J Biol Chem*. 1994;269:2111–2117.

14. MacDonald IM, Russell L, Chan CC. Choroideremia: new findings from ocular pathology and review of recent literature. *Surv Ophthalmol*. 2009;54:401–407.

15. Flannery JG, Bird AC, Farber DB, Weleber RG, Bok D. A histopathologic study of a choroideremia carrier. *Invest Ophthalmol Vis Sci*. 1990;31:229–236.

16. Syed N, Smith JE, John SK, Seabra MC, Aguirre GD, Milam AH. Evaluation of retinal photoreceptors and pigment epithelium in a female carrier of choroideremia. *Ophthalmology*. 2001; 108:711–720.

17. Tolmachova T, Wavre-Shapton ST, Barnard AR, MacLaren RE, Futter CE, Seabra MC. Retinal pigment epithelium defects accelerate photoreceptor degeneration in cell type-specific knockout mouse models of choroideremia. *Invest Ophthalmol Vis Sci*. 2010;51:4913–4920.

18. Cameron JD, Fine BS, Shapiro I. Histopathologic observations in choroideremia with emphasis on vascular changes of the uveal tract. *Ophthalmology*. 1987;94:187–196.

19. Ghosh M, McCulloch JC. Pathological findings from two cases of choroideremia. *Can J Ophthalmol*. 1980;15:147–153.

20. McCulloch JC. The pathologic findings in two cases of choroideremia. *Trans Am Acad Ophthalmol Otolaryngol*. 1950;54:565–572.

21. Jacobson SG, Cideciyan AV, Sumaroka A, et al. Remodeling of the human retina in choroideremia: rab escort protein 1 (REP-1) mutations. *Invest Ophthalmol Vis Sci*. 2006;47:4113–4120.

22. Roorda A. Applications of adaptive optics scanning laser ophthalmoscopy. *Optom Vis Sci*. 2010;87:260–268.

23. Duncan JL, Zhang Y, Gandhi J, et al. High-resolution imaging with adaptive optics in patients with inherited retinal degeneration. *Invest Ophthalmol Vis Sci*. 2007;48:3283–3291.

24. Genead MA, Fishman GA, Rha J, et al. Photoreceptor structure and function in patients with congenital achromatopsia. *Invest Ophthalmol Vis Sci*. 2011;52:7298–7308.

25. Godara P, Rha J, Tait DM, et al. Unusual adaptive optics findings in a patient with bilateral maculopathy. *Arch Ophthalmol*. 2010;128:253–254.

26. Rha J, Dubis AM, Wagner-Schuman M, et al. Spectral domain optical coherence tomography and adaptive optics: imaging photoreceptor layer morphology to interpret preclinical phenotypes. *Adv Exp Med Biol*. 2010;664:309–316.

27. Wolfing JI, Chung M, Carroll J, Roorda A, Williams DR. High-resolution retinal imaging of cone-rod dystrophy. *Ophthalmology*. 2006;1131019;e1011.

28. Yoon MK, Roorda A, Zhang Y, et al. Adaptive optics scanning laser ophthalmoscopy images in a family with the mitochondrial DNA T8993C mutation. *Invest Ophthalmol Vis Sci*. 2009; 50:1838–1847.

29. MacDonald IM, Sereda C, McTaggart K, Mah D. Choroideremia gene testing. *Expert Rev Mol Diagn*. 2004;4:478–484.

30. Sharp A, Robinson D, Jacobs P. Age- and tissue-specific variation of X chromosome inactivation ratios in normal women. *Hum Genet*. 2000;107:343–349.

31. Dagnelie G. Conversion of planimetric visual field data into solid angles and retinal areas. *Clin Vision Sci*. 1990;5:95–100.

32. Duncan JL, Talcott KE, Ratnam K, et al. Cone structure in retinal degeneration associated with mutations in the peripherin/RDS gene. *Invest Ophthalmol Vis Sci*. 2011;52:1557–1566.

33. Marmor MF, Holder GE, Seeliger MW, Yamamoto S. Standard for clinical electroretinography (2004 update). *Doc Ophthalmol*. 2004;108:107–114.

34. Cooper RF, Dubis AM, Pavaskar A, Rha J, Dubra A, Carroll J. Spatial and temporal variation of rod photoreceptor reflectance in the human retina. *Biomed Opt Express*. 2011;2:2577–2589.

35. Dubra A, Sulai Y, Norris JL, et al. Noninvasive imaging of the human rod photoreceptor mosaic using a confocal adaptive optics scanning ophthalmoscope. *Biomed Opt Express*. 2011; 2:1864–1876.

36. Zhang Y, Poonja S, Roorda A. MEMS-based adaptive optics scanning laser ophthalmoscopy. *Opt Lett*. 2006;31:1268–1270.

37. Vogel CR, Arathorn DW, Roorda A, Parker A. Retinal motion estimation in adaptive optics scanning laser ophthalmoscopy. *Opt Express*. 2006;14:487–497.

38. Rha J, Schroeder B, Godara P, Carroll J. Variable optical activation of human cone photoreceptors visualized using a short coherence light source. *Opt Lett*. 2009;34:3782–3784.

39. Coletta NJ, Williams DR. Psychophysical estimate of extrafoveal cone spacing. *J Opt Soc Am A*. 1987;4:1503–1513.

40. Williams DR, Coletta NJ. Cone spacing and the visual resolution limit. *J Opt Soc Am A*. 1987;4:1514–1523.

41. Srinivasan VJ, Monson BK, Wojtkowski M, et al. Characterization of outer retinal morphology with high-speed, ultrahigh-resolution optical coherence tomography. *Invest Ophthalmol Vis Sci*. 2008;49:1571–1579.

42. Spaide RF, Curcio CA. Anatomical correlates to the bands seen in the outer retina by optical coherence tomography: literature review and model. *Retina*. 2011;31:1609–1619.

43. Zweifel SA, Engelbert M, Laud K, Margolis R, Spaide RF, Freund KB. Outer retinal tubulation: a novel optical coherence tomography finding. *Arch Ophthalmol*. 2009;127:1596–1602.

44. Genead MA, Fishman GA. Cystic macular oedema on spectral-domain optical coherence tomography in choroideremia patients without cystic changes on fundus examination. *Eye (Lond)*. 2011;25:84–90.

45. Bonilha VL, Trzupek KM, Li Y, et al. Choroideremia: analysis of the retina from a female symptomatic carrier. *Ophthalmic Genet*. 2008;29:99–110.

46. Cheung MC, Nune GC, Wang M, McTaggart KE, MacDonald IM, Duncan JL. Detection of localized retinal dysfunction in a choroideremia carrier. *Am J Ophthalmol*. 2004;137:189–191.

47. Roorda A, Zhang Y, Duncan JL. High-resolution in vivo imaging of the RPE mosaic in eyes with retinal disease. *Invest Ophthalmol Vis Sci*. 2007;48:2297–2303.

48. Seabra MC, Mules EH, Hume AN. Rab GTPases, intracellular traffic and disease. *Trends Mol Med*. 2002;8:23–30.

49. Lazow MA, Hood DC, Ramachandran R, et al. Transition zones between healthy and diseased retina in choroideremia (CHM) and Stargardt disease (STGD) as compared to retinitis pigmentosa (RP). *Invest Ophthalmol Vis Sci*. 2011;52:9581–9590.

50. Mura M, Sereda C, Jablonski MM, MacDonald IM, Iannaccone A. Clinical and functional findings in choroideremia due to complete deletion of the CHM gene. *Arch Ophthalmol*. 2007;125:1107–1113.

51. Preising MN, Wegscheider E, Friedburg C, Poloschek CM, Wabbels BK, Lorenz B. Fundus autofluorescence in carriers of choroideremia and correlation with electrophysiologic and psychophysical data. *Ophthalmology*. 2009;116:1201–1209.e1201–e1202.

52. Drexler W, Fujimoto JG. State-of-the-art retinal optical coherence tomography. *Prog Retin Eye Res*. 2008;27:45–88.

53. Zawadzki RJ, Choi SS, Fuller AR, Evans JW, Hamann B, Werner JS. Cellular resolution volumetric in vivo retinal imaging with adaptive optics-optical coherence tomography. *Opt Express*. 2009;17:4084–4094.

54. Zawadzki RJ, Jones SM, Pilli S, et al. Integrated adaptive optics optical coherence tomography and adaptive optics scanning laser ophthalmoscope system for simultaneous cellular resolution in vivo retinal imaging. *Biomed Opt Express*. 2011;2:1674–1686.

55. Sergouniotis PI, Davidson AE, Lenassi E, Devery SR, Moore AT, Webster AR. Retinal structure, function, and molecular pathologic features in gyrate atrophy. *Ophthalmology*. 2012;119:596–605.

56. Pennesi ME, Weleber RG. High-resolution optical coherence tomography shows new aspects of Bietti crystalline retinopathy. *Retina*. 2010;30:531–532.

57. Del Priore LV, Kuo YH, Tezel TH. Age-related changes in human RPE cell density and apoptosis proportion in situ. *Invest Ophthalmol Vis Sci*. 2002;43:3312–3318.

58. Dorey CK, Wu G, Ebenstein D, Garsd A, Weiter JJ. Cell loss in the aging retina. Relationship to lipofuscin accumulation and macular degeneration. *Invest Ophthalmol Vis Sci*. 1989;30:1691–1699.

59. Gao H, Hollyfield JG. Aging of the human retina. Differential loss of neurons and retinal pigment epithelial cells. *Invest Ophthalmol Vis Sci*. 1992;33:1–17.

60. Panda-Jonas S, Jonas JB, Jakobczyk-Zmija M. Retinal pigment epithelial cell count, distribution, and correlations in normal human eyes. *Am J Ophthalmol*. 1996;121:181–189.

61. Watzke RC, Soldevilla JD, Trune DR. Morphometric analysis of human retinal pigment epithelium: correlation with age and location. *Curr Eye Res*. 1993;12:133–142.

62. Morgan JI, Dubra A, Wolfe R, Merigan WH, Williams DR. In vivo autofluorescence imaging of the human and macaque retinal pigment epithelial cell mosaic. *Invest Ophthalmol Vis Sci*. 2009;50:1350–1359.

63. Godara P, Dubis AM, Roorda A, Duncan JL, Carroll J. Adaptive optics retinal imaging: emerging clinical applications. *Optom Vis Sci*. 2010;87:930–941.